GSA Data Repository 2017323

Delano, J.E., Amos, C.B., Loveless, J.P., Rittenour, T.M., Sherrod, B.L., Lynch, E.M., 2017, Influence of the megathrust earthquake cycle on upper plate deformation in the Cascadia forearc of Washington State: Geology, doi: 10.1130/G39070.1

Contents

APPENDIX DR1: ADDITIONAL METHODOLOGICAL DETAILS

Optically Stimulated Luminescence (OSL) Dating

Outwash and strath terrace deposits along the length of the Wynoochee River were dated using small aliquot, regenerative-dose (SAR; Murray and Wintle, 2000) (Figs. DR1-DR8). Samples were collected in terraces cut by mapped fault scarps, to constrain earthquake timing and slip rates, as well as from the most continuous terraces in the study area, to calculate incision rates. Sample sites were chosen in exposures that showed clear fluvial lateral accretion structures (cross-bedding), targeting sediment containing the highest proportion of fine sand. Samples were collected following standard procedures (e.g., Nelson et al., 2015) by pounding opaque steel tubes horizontally into the targeted material after clearing back the outer 10 cm of sediment from the outcrop face. Sediment from a 30 cm radius around the sample tube was collected at each site for water content and radio-elemental concentration for calculation of environmental dose rate analysis. Sample depth was recorded for cosmic contribution to the dose rate.

All sample preparation and analyses were performed at Utah State University under amber light (590 nm wavelength). Each sample was wet sieved to target fine sand and treated with hydrochloric acid (10% HCl) and bleach (10% H_2O_2) to remove carbonate and organic material. Quartz grains were separated from heavy minerals using sodium polytungstate (2.7 g/cm^3). Quartz grains were then treated with concentrated hydrofluoric acid (47% HF) to remove feldspar and etch the outer grain. Moisture content was measured by calculating the weight difference between damp field sediment and the dried sample. The environmental dose rate of each sample was determined by chemical analysis of the K, Rb, U, and Th content using ICP-MS and ICP-AES techniques and conversion factors of Guérin et al. (2011). The contribution of cosmic radiation to the dose rate was calculated using sample depth, elevation, and

latitude/longitude following Prescott and Hutton (1994). Dose rates are calculated based on water content, sediment chemistry, and cosmic contribution (Aitken and Xie, 1990; Aitken, 1998). The final equivalent dose (De) used for age calculation was determined using a minimum age model (MAM, Galbraith and Roberts, 2012) in order to isolate the populate of grains exposed to light prior to deposition.

One concern with the application of OSL dating in fluvial environments is the potential for partial bleaching (incomplete resetting), resulting in artificially old depositional ages (e.g., Rittenour, 2008). To help identify problems with partial bleaching we collected paired samples (e.g., WYN-15 and WYN-16 are pairs) from the same exposure (or in very close proximity) within the same terrace. WYN-07 and WYN-08 are the only samples that were not collected with an adjoining sample due to limited appropriate material for sampling. This double-sample method was employed to increase the chance of identifying partially bleached samples, account for potential problems with the luminescence signal or dose rate calculation for a sample, and reduce age uncertainty caused by the lack of outside age controls (such as radiocarbon dating) we had available in this study.

Many of the collected sample pairs yielded measurable luminescence for only one sample of the pair (Table DR1). WYN-19 yields a burial age for Qt8 of 7.8 ± 2.4 ka, and WYN-04 yields an age of 8.9 ± 2.4 ka for Qt7. Of the viable samples collected in unit Qt5, two are from the same outcrop. These paired samples (WYN-15 and WYN-16) yield ages of 13.5 ± 4.0 ka and 13.5 ± 6.3 ka, respectively. These ages generally agree with samples from other outcrops of Qt5, which produced age estimates of 14.6 ± 3.5 ka (WYN-07), 14.8 ± 4.0 ka (WYN-06), and 22.9 ± 6.2 ka (WYN-08). The sample from Qt4 yielded an age of 32.2 ± 9.7 ka (WYN-17).

We chose not to use WYN-18 for analysis because the luminescence results appear unreliable. Since samples WYN-17 and WYN-18 were collected from essentially the same location but have vastly different luminescence results, it is likely that one result does not represent the burial age of the deposit. Sample WYN-18 had very poor luminescence characteristics during lab processing and presented many problems during analysis, has a large relative error of (44%). Additionally, a much smaller proportion of WYN-18 aliquots were accepted (relative to the total number of disks analyzed) (Table DR1) during age calculation compared to WYN-17. These results are also consistent with the mapped locations and elevations of Qt4 relative to other terraces. Therefore, we chose not to use WYN-18 in slip rate analyses and instead utilize the age results from WYN-17 for Qt4.

We use these singular sample ages for separation rate calculations. For Qt5, which has multiple samples, we use the WYN-06 sample age because it was collected from the same terrace exposure as the scarp profiles.

OSL samples were collected 1-4 m below the terrace tread (Table DR 1) and are capped by additional gravel and loess. Therefore, sample burial predates modern tread formation and OSL ages and generate minimum slip rates. However, the time difference between sample burial and the modern tread formation is likely negligible within the OSL age uncertainty.

Our OSL sample ages suggest terrace deposition correlates with increased sediment supply associated with glacial maxima, and agree with ages seen in other Olympic Mountain drainages (Pazzaglia and Brandon, 2001; Wyshnytzky et al., 2014). One Qt5 sample, however (WYN-08, 22.9 ± 6.2 ka), is similar in age to Qt4, a stratigraphically older deposit. This apparent discrepancy may be a result of partial bleaching of sample WYN-08, or reflect multiple terrace deposits on the same strath. For incision rate calculations, we use an arithmetic mean of OSL

ages from the four youngest Qt5 OSL samples, excluding the oldest age that likely represents partial bleaching (See Table DR1). Incision rates are calculated by dividing the height of the strath by the average age, with standard error propagation. The choice to use an average age, rather than choosing a singular sample age, reflects the uncertainty between sediment burial ages at different sample sites. Key to these calculations, however, is the assumption that all treads were abandoned simultaneously in favor of vertical incision. We calculate a reduced chi squared value of 0.23, which suggests the age scatter can be explained with analytical 1σ uncertainties (e.g., Schaefer et al., 2009). The arithmetic mean of these four sample ages yields a Qt5 deposit age of 14.1 ± 0.6 (1σ uncertainty).

Boundary Element Method Model

We use a geodetically constrained elastic block model (Meade and Loveless, 2009; available at https://github.com/jploveless/Blocks), with boundaries of microplates defined by active (Holocene) faults and gradients in GPS velocities (Loveless and Meade, 2011a; Evans et al., 2015). We use a composite velocity field comprising 1717 stations from 6 published fields (Shen et al., 2003; Hammond and Thatcher, 2005; Williams et al., 2006; McCaffrey et al., 2013; Plate Boundary Observatory network velocity field, http://pboweb.unavco.org), rotated using a six-parameter (rotation plus translation) transformation into the reference frame of McCaffrey et al. (2013). We simultaneously estimate microplate rotations about Euler poles and elastic deformation arising from fully coupled block boundaries and from spatially variable coupling on the Cascadia subduction zone (CSZ). The relative motion between the Juan de Fuca and North American plates is defined using the Euler pole of Miller et al. (2001). We parameterize the CSZ as a continuous network of triangular dislocation elements (TDEs), capable of representing along

strike and down dip geometric complexity; the shape of the CSZ is based on the slab contours defined by McCrory et al. (2009).

To regularize the inversion of geodetic velocities for spatially variable slip deficit on the CSZ, we impose a Laplacian smoothing constraint, varying the weighting of the smoothing operator proportional to the resolving capability of the geodetic velocities (Loveless and Meade, 2011b). We test a range of nominal smoothing weights in order to explore the sensitivity of the estimated slip deficit to this assumption, finding that the boundary element results described below are generally consistent across the range. The formal smoothing constraint we use is the smallest that yields estimated slip deficit rate values no larger than the long-term slip rate from plate convergence (i.e., 100% coupled). The resulting coupling distribution is similar to those published by Evans et al. (2015; their Figure 15c), McCaffrey et al. (2013; their Figure 6a), and Schmalzle et al. (2014; their Figure 6b). Using our smoothing constraint, we carry out a Monte Carlo simulation to estimate uncertainties in the slip deficit rate. We invert 5000 realizations of the velocity field arising from the estimated slip deficit distribution, perturbed by noise proportional to the GPS station uncertainties. These estimated uncertainties on the slip deficit distribution are propagated into the boundary element model, described below, to yield uncertainties on the forward calculation of interseismic uplift rate in the Wynoochee River valley region (Figure 3 of the main text).

We use the estimated CSZ slip deficit rate distribution as an input condition in a boundary element method model (e.g., Crouch and Starfield, 1983) to calculate the stress rate imposed on the forearc by interseismic megathrust coupling. The boundary element code and input files are available at https://github.com/jploveless/tribem. We calculate stress rate analytically (Meade, 2007) in a homogeneous elastic half space characterized by a shear modulus

3×10^{10} Pa and Poisson's ratio of 0.25 with embedded TDEs that represent the Canyon River fault (CRF). On each TDE in the model, we prescribe displacement (slip) rate or traction rate in the element strike, element dip, and element normal directions. On the CSZ TDEs, we prescribe the geodetically estimated slip deficit rate in the strike and dip directions. On the CRF TDEs, we prescribe zero shear traction in the strike and dip directions. On all TDEs, we prescribe zero displacement rate conditions in the element-normal direction to prevent opening or interpenetration across elements. Slip deficit rate conditions on the CSZ TDEs result in stress throughout the elastic half space, including traction resolved on the CRF elements. We then estimate the slip rate distribution on the CRF necessary to achieve the prescribed zero shear traction rate conditions, which we interpret as the slip rate distribution required to relieve the shear traction imposed by CSZ coupling (Fig. DR10). The GPS velocity field used to constrain the coupling distribution on the CSZ is insufficiently dense to resolve short-wavelength asperities on the subduction interface given the smoothing-based regularization. It is possible that such asperities exist and induce localized perturbations to the crustal stress field, including stress resolved on the CRF, which in turn would impact the estimated CRF slip distribution, but we cannot identify such features using currently available data.

Displacement fields are calculated at observation coordinates in the Wynoochee River valley region, as well as along the valley profile, using the slip deficit on the CSZ and the estimated slip on the CRF (Fig. DR11). We also test an isostatic adjustment to predicted uplift values, using a model of flexure of elastic crust over a viscous mantle (e.g., Turcotte and Schubert, 2002). We use a mantle density of 4100 kg/m^3, crustal density of 2700 kg/m^3, and a flexural rigidity of the crust of 2×10^{23} Pa·m^3, following previous applications of this adjustment (Cooke and Dair, 2011; Fattaruso et al., 2014). We find little difference between the raw (Fig.

DR11) and adjusted vertical displacements (Fig. DR12), with a max uplift difference of 0.37 mm/yr.

Alternative Geometry

We tested alternative fault configurations using the boundary element method model to understand how uncertainty in fault geometry affects modeled slip on the CRF. We varied fault depth and fault connectivity to evaluate potential differences in dip-slip and uplift rates.

Changes in fault projection depth: We tested fault depth variation by projecting the surface trace to 5 km, 10 km, or 15 km depth. The predicted peak slip rate value along the CRF is dependent on fault depth. The maximum dip-slip rates for 5, 10, and 15 km fault depths are 0.4 mm/yr, 0.65 mm/yr, and 0.8 mm/yr, respectively. The spatial slip distribution along the fault plane remains similar, but slip magnitudes scale with depth.

Changes in fault connectivity: To test alternative fault connectivity at depth, we connected the two largest fault segments into one fault plane and left two smaller mapped segments disconnected. Connecting the two largest fault segments partitions slip off of small segments and increasing peak slip in those connected regions. For faults projected to the same depth, the disconnected scenario slips more on small segments than the connected scenario. Additionally, the uplift pattern becomes more uniform in a connected fault system. With a disconnected fault trace projected to 10 km depth, uplift is very low (~0.1-0.15 mm/yr) near the Wynoochee River valley, a stark contrast to the maximum values nearing ~0.4 mm/yr with a connected fault trace. The minimum uplift in the Wynoochee River valley with a continuous fault trace (~0.2-0.3 mm/yr) is not as pronounced as in the segmented model, but it remains a local minimum nonetheless.

Scaling fault depth with fault length: We also modeled slip on the CRF with variable fault depth along the trace. Shorter fault segments were projected to 5 km depth, while longer fault segments were projected to 10 km fault depth. Using this method, we modeled slip for a disconnected fault trace as well as connecting the two largest segments. Variable fault depth did not significantly affect fault slip rates or uplift patterns.

Therefore, we conclude that although the fault geometry is uncertain, the first-order conclusions drawn in the main text are insignificantly affected by perturbations to the geometry.

Synthetic Subduction Zone Earthquake

We also simulated a CSZ earthquake and estimated the resulting slip distribution on the CRF (Figs. DR13-DR14) to address other studies (e.g., Mazzotti et al., 2002; Sherrod and Gomberg, 2014) that suggested CSZ coseismic slip could initiate slip on upper plate faults like the CRF. We tested many different moderately-sized CSZ earthquake scenarios, varying both initiation depth and location along strike and holding peak slip constant at 1 m. The four earthquake examples presented (Fig. DR13) most influenced slip on the CRF. CSZ coseismic slip produced normal dip-slip on the southeast-dipping CRF (Fig. DR14).

Scarp and Longitudinal Profiling

We calculate relative surface deformation across the fault as well as terrace incision by creating topographic profiles extracted from the lidar data (where vertical accuracy is 0.05 m). Fault scarp profiles (A-P, X) are measured orthogonally to fault trace orientation. Dip slip displacements and associated uncertainties are calculated using the Monte Carlo method (100k realizations) following Thompson et al., (2002), varying fault location with equal probability between ½ and ⅓ the scarp height. The fault dip range (55°-85°) reflects the estimated 70° dip from Walsh and Logan, (2007), with equal probability of dip varying ± 15°. The error

contribution from the lidar data is at least 1 order of magnitude less than the error calculated from scarp profiles, and is therefore negligible at cm-scale precision used in displacement calculations. We use dip values from Walsh and Logan (2007) because the fault's segmentation and frequent step-overs within the Wynoochee valley make accurate fault dip calculations using a 3-point problem difficult and potentially inaccurate. Over the entire length of the fault, the intersection of the fault trace with topographic landforms (e.g. terrace risers, canyons, etc.) is generally consistent with a steeply south-dipping fault. Our 3-point problem approximations in more slightly more continuous fault segments yield dip values of ~75°SE, consistent with Walsh and Logan (2007) trenching results.

The Qt4 terrace tread shows evidence of alluvial fan deposition post-dating terrace formation. Thus, the OSL age of the terrace surface is older than the displacement recorded in alluvial fan surface. Therefore, vertical separation values and estimated slip rates from profiles K-P are minima.

For longitudinal Qt5 profiles along the entire river (Fig. 3 of main text) we use valley distance, measured north to south following the central axis of the Wynoochee River valley as in Pazzaglia and Brandon (2001). Valley distance, compared to river distance, removes short-length variation caused by river meanders and allows direct elevation comparison of terraces projected from both sides of the valley. To create terrace tread valley profiles, individual terrace profiles were mapped and assigned elevations derived from the lidar. Tread profile lines were converted to elevation points spaced 10 m apart and projected orthogonally to the valley profile line. Individual strath elevation observations were also projected orthogonally to the same valley line.

DATA REPOSITORY REFERENCES CITED

Aitken, M.J. 1998: An Introduction to Optical Dating: The dating of Quaternary sediments by the use of photon-stimulated luminescence. New York, Oxford University Press, 267 p.
Aitken, M.J., Xie, J., 1990. Moisture correction for annual gamma dose. Ancient TL 8 (2), 6-9.
Cooke, M.L. and Dair, L.C., 2011, Simulating the recent evolution of the southern big bend of the San Andreas fault, Southern California, Journal of Geophysical Research, v. 116, B04405, doi:10.1029/2010JB007835.
Crouch, S. L., and A. M. Starfield, 1983, Boundary Element Methods in Solid Mechanics, Allen and Unwin, London.
Evans, E.L., Loveless, J.P., and Meade, B.J., 2015, Total variation regularization of geodetically and geologically constrained block models for the Western United States: Geophysical Journal International, v. 202, no. 2, p. 713–727, doi: 10.1093/gji/ggv164.
Fattaruso, L.A., Cooke, M.L., and Dorsey, R.J., 2014, Sensitivity of uplift patterns to dip of the San Andreas fault in the Coachella Valley, California, Geosphere, v. 10, no. 6, p. 1235–1246.
Galbraith, R.F., Roberts, R.G., 2012. Statistical aspects of equivalent dose and error calculation and display in OSL dating: An Overview and some recommendations. Quaternary Geochronology 11, 1-27.
Guérin, G., Mercier, N., Adamiec, G., 2011. Dose-rate conversion factors: update: Ancient TL 29, 5-8.
Hammond, W.C., and Thatcher, W., 2005, Northwest Basin and Range tectonic deformation observed with the Global Positioning System, 1999–2003: Journal of geophysical research., v. 110, no. B10, doi: 10.1029/2005JB003678.
Loveless, J.P. and Meade, B.J. (2011a), Stress modulation on the San Andreas fault due to interseismic fault system interactions, Geology, v. 39, no. 11, p. 1035–1038, doi:10.1130/G32215.1.
Loveless, J.P. and Meade, B.J. (2011b), Spatial correlation of interseismic coupling and coseismic rupture extent of the 2011 M_W=9.0 Tohoku-oki earthquake, Geophysical Research Letters, v. 38, L17306, doi:10.1029/2011GL048561.
Mazzotti, S., Dragert, H., Hyndman, R.D., Miller, M.M., and Henton, J.A., 2002, GPS deformation in a region of high crustal seismicity: N. Cascadia forearc: Earth and Planetary Science Letters, v. 198, no. 1–2, p. 41–48, doi: 10.1016/S0012-821X(02)00520-4.
McCaffrey, R., King, R.W., Payne, S.J., and Lancaster, M., 2013, Active tectonics of northwestern U.S. inferred from GPS-derived surface velocities: Journal of Geophysical Research: Solid Earth, v. 118, no. 2, p. 709–723, doi: 10.1029/2012JB009473.
McCrory, P.A., Blair, J.L., Oppenheimer, D.H. & Walter, S.R., 2009. Depth to the Juan de Fuca slab beneath the Cascadia subduction margin—a 3-D model sorting earthquakes, U.S. Geological Survey Data Series 91, Version 1.2.
Meade, B.J., 2007, Present-day kinematics at the India-Asia collision zone: Geology, v. 35, no. 1, p. 81–84, doi: 10.1130/G22924A.1.
Meade, B.J., and Loveless, J.P., 2009, Block Modeling with Connected Fault-Network Geometries and a Linear Elastic Coupling Estimator in Spherical Coordinates: Bulletin of the Seismological Society of America, v. 99, no. 6, p. 3124–3139, doi: 10.1785/0120090088.
Miller, M.M., Johnson, D.J., Rubin, C.M., Dragert, H., Wang, K., Qamar, A. & Goldfinger, C., 2001. GPS-determination of along-strike variation in Cascadia margin kinematics:

implications for relative plate motion, subduction zone coupling, and permanent deformation, Tectonics, v. 20, no. 2, p. 161–176.
Murray, A.S., Wintle, A.G., 2000. Luminescence dating of quartz using an improved single aliquot regenerative-dose protocol. Radiation Measurements 32, 57-73.
Nelson, M.S., Gray, H.J., Johnson, J.A., Rittenour, T.M., Feathers, J.K., Mahan, S., 2015, User guide for luminescence sampling in archaeological and geological context. Advances in Archaeological Practice. 3, 166-177
Pazzaglia, F.J., and Brandon, M.T., 2001, A Fluvial Record of Long-term Steady-state Uplift and Erosion Across the Cascadia Forearc High, Western Washington State: American Journal of Science, v. 301, no. 4–5, p. 385–431, doi: 10.2475/ajs.301.4-5.385.
Prescott, J. R., Hutton, J.T., 1994. Cosmic ray contributions to dose rates for luminescence and ESR dating: Radiation Measurements 23, 497-500.
Rittenour, T.M., 2008, Luminescence dating of fluvial deposits: applications to geomorphic, palaeoseismic and archaeological research. Boreas 37, 613-635.
Schaefer, J. M., Denton, G. H, Kaplan, M. Putnam, A., Finkel, R. C., Barrell, D. J. A, Andersen, B. G., Schwartz, R., Mackintosh, A., Chinn, T., Schlüchter, C., 2009. High-Frequency Holocene Glacier Fluctuations in New Zealand Differ from the Northern Signature, Science, v. 324, no. 5927, p. 622-625, DOI: 10.1126/science.1169312.
Schmalzle, G. M., R. McCaffrey, and K. C. Creager, 2014, Central Cascadia subduction zone creep: Geochemistry, Geophysics, Geosystems, v. 15, p. 1515–1532, doi:10.1002/2013GC005172.
Shen Jun, Wang Yipeng, and Song Fangmin, 2003, Characteristics of the active Xiaojiang fault zone in Yunnan, China: a slip boundary for the southeastward escaping Sichuan–Yunnan Block of the Tibetan Plateau: Journal of Asian Earth Sciences, v. 21, no. 10, p. 1085–1096, doi: 10.1016/S1367-9120(02)00185-2.
Sherrod, B., and Gomberg, J., 2014, Crustal earthquake triggering by pre-historic great earthquakes on subduction zone thrusts: Journal of Geophysical Research. Solid Earth, v. 119, p. 1273–1294, doi:10.1002/2013JB010635.
Thompson, S.C., Weldon, R.J., Rubin, C.M., Abdrakhmatov, K., Molnar, P., and Berger, G.W., 2002, Late Quaternary slip rates across the central Tien Shan, Kyrgyzstan, central Asia: Journal of Geophysical Research: Solid Earth, v. 107, no. B9, p. 2203, doi: 10.1029/2001JB000596.
Turcotte, D.L. and Schubert, G., 2002, Geodynamics: New York, Cambridge University Press, 456 p.
Walsh, T.J., and Logan, R.L., 2007, Results of trenching the Canyon River fault, southeast Olympic Mountains, Washington: GSA Annual meeting, Cordilleran Section, poster No. 22-4.
Williams, T.B., Kelsey, H.M., and Freymueller, J.T., 2006, GPS-derived strain in northwestern California: Termination of the San Andreas fault system and convergence of the Sierra Nevada–Great Valley block contribute to southern Cascadia forearc contraction: Tectonophysics, v. 413, no. 3–4, p. 171–184, doi: 10.1016/j.tecto.2005.10.047.
Wyshnytzky, C.E., Rittenour, T.M., Nelson, M.S., and Thackray, G., 2014, Luminescence dating of late Pleistocene proximal glacial sediments in the Olympic Mountains, Washington: Quaternary International, v. 362, p. 116–123, doi: 10.1016/j.quaint.2014.08.024.

TABLE DR1. OPTICALLY STIMULATED LUMINESCENCE SAMPLE RESULTS

Sample number	USU number	Map unit	Location Lat (°N)	Location Long (°W)	Elevation (m)	Burial depth (m)	Valley distance (km)	Number aliquots*	Dose rate ± 2σ (Gy/ka)	$D_E^{\dagger}$ ± 2σ (Gy)	OD[§] ± 2σ (%)	Age ± 2σ (ka)
WYN-04	2054	Qt7	47.3423	123.6409	165	2.5	5.75	21 (42)	0.87 ± 0.08	8.6 ± 2.1	31.0 ± 7.0	8.9 ± 2.4
WYN-06	2056	Qt5	47.3417	123.6507	194	1.0	6.03	17 (31)	1.00 ± 0.07	15.5 ± 3.9	0.0	14.8 ± 4.0
WYN-07	2057	Qt5b	47.1006	123.6848	57	3.5	34.96	15 (24)	0.71 ± 0.04	10.4 ± 2.3	37.7 ± 8.7	14.6 ± 3.5
WYN-08	2058	Qt5	47.0583	123.6928	42	1.5	39.79	21 (31)	1.11 ± 0.06	25.3 ± 6.4	18.0 ± 5.5	22.9 ± 6.2
WYN-15	2065	Qt5	47.2121	123.6355	107	2.0	20.91	14 (56)	0.87 ± 0.05	11.8 ± 5.4	14.2 ± 13.1	13.5 ± 6.3
WYN-16	2066	Qt5	47.2121	123.6355	109	1.5	20.91	16 (40)	0.82 ± 0.05	11.0 ± 3.0	26.1 ± 7.6	13.5 ± 4.0
WYN-17	2067	Qt4	47.3740	123.6147	253	1.5	1.17	25 (37)	0.95 ± 0.10	30.6 ± 8.7	35.5 ± 7.1	32.2 ± 9.7
WYN-18	2068	Qt4	47.3740	123.6147	253	1.5	1.17	9 (31)	0.85 ± 0.05	12.5 ± 5.6	0.0	14.7 ± 6.7
WYN-19	2069	Qt8	47.3419	123.6407	162	1.5	5.82	18 (27)	1.12 ± 0.06	8.7 ± 2.6	20.5 ± 6.6	7.8 ± 2.4

*Age analysis using the single-aliquot regenerative-dose procedure of Murray and Wintle (2000) on 2-5mm small-aliquots of quartz sand. Number of aliquots used in age calculation and number of aliquots analyzed in parentheses.

[†]Equivalent dose (DE) calculated using the Minimum Age Model (MAM) of Galbraith and Roberts (2012).

[§]Overdispersion (OD) epresents variance in DE data beyond measurement uncertainties, OD >20% may indicate significant scatter due to depositional or post-depositional processes

TABLE DR2. OPTICALLY STIMULATED LUMINESCENCE DOSE RATE RESULTS

Sample number	USU number	In-situ H20* (%)	Grain size (μm)	K† (%)	Rb† (ppm)	Th† (ppm)	U† (ppm)	Cosmic (Gy/ka)
WYN-04	2054	22.4	90-150	0.66 ± 0.02	21.4 ± 0.9	1.7 ± 0.2	0.5 ± 0.1	0.16 ± 0.02
WYN-06	2056	15.6	90-150	0.69 ± 0.02	19.3 ± 0.8	1.9 ± 0.2	0.5 ± 0.1	0.19 ± 0.02
WYN-07	2057	5.2	125-250	0.48 ± 0.01	9.3 ± 0.4	1.1 ± 0.2	0.4 ± 0.1	0.14 ± 0.01
WYN-08	2058	7.5	150-250	0.78 ± 0.02	26.0 ± 1.0	1.9 ± 0.2	0.6 ± 0.1	0.17 ± 0.02
WYN-15	2065	11.2	150-250	0.60 ± 0.02	14.7 ± 0.6	1.3 ± 0.2	0.5 ± 0.1	0.16 ± 0.02
WYN-16	2066	5.7	150-250	0.54 ± 0.01	16.0 ± 0.6	1.3 ± 0.2	0.4 ± 0.1	0.18 ± 0.02
WYN-17	2067	4.8	150-250	0.65 ± 0.02	11.7 ± 0.5	1.5 ± 0.2	0.5 ± 0.1	0.18 ± 0.02
WYN-19	2069	4.4	90-180	0.78 ± 0.02	26.3 ± 1.1	1.2 ± 0.2	0.5 ± 0.1	0.18 ± 0.02

*Assume 10±3% for moisture content over burial history for all samples.

†Radioelemental concentrations determined by ALS Chemex using ICP-MS and ICP-AES techniques; dose rate is derived from concentrations by conversion factors from Guerin et al. 2011.

TABLE DR3. CANYON RIVER FAULT SCARP PROFILE RESULTS

Profile	Location Lat (°N)	Location Long (°W)	Elevation (m)	Unit	Distance along scarp (m)	Fault dip range (°)	Vertical separation (Vs) (m)	Dip slip (Ds) (m)	Vs rate[§] (mm/yr)	Ds rate[§] (mm/yr)	OSL sample	Age (ka)
A	47.3394	123.6470	179.4	Qt6	28	55-85	1.61 + 0.78 - 0.79	1.73 + 0.89 - 0.85	n/a[†]	n/a[†]	n/a[†]	n/a[†]
B	47.3397	123.6468	179.3	Qt6	68	55-85	1.56 + 0.41 - 0.41	1.69 + 0.50 - 0.47	n/a[†]	n/a[†]	n/a[†]	n/a[†]
C	47.3399	123.6466	179.7	Qt6	104	55-85	1.65 + 0.54 - 0.54	1.79 + 0.63 - 0.60	n/a[†]	n/a[†]	n/a[†]	n/a[†]
D	47.3404	123.6461	180.2	Qt6	160	55-85	1.70 + 0.59 - 0.60	1.83 + 0.70 - 0.66	n/a[†]	n/a[†]	n/a[†]	n/a[†]
E	47.3413	123.6445	168.1	Qt7	327	55-85	0.92 + 0.51 - 0.52	1.00 + 0.58 - 0.56	0.10 + 0.08 - 0.06	0.11 + 0.09 - 0.06	WYN-04	8.9 ± 1.2
F	47.3416	123.6442	167.9	Qt7	362	55-85	1.48 + 0.56 - 0.56	1.60 + 0.65 - 0.61	0.16 + 0.10 - 0.06	0.17 + 0.11 - 0.06	WYN-04	8.9 ± 1.2
G	47.3429	123.6402	167.5	Qt7	701	55-85	2.95 + 1.13 - 1.11	3.20 + 1.31 - 1.23	0.32 + 0.20 - 0.12	0.35 + 0.21 - 0.13	WYN-04	8.9 ± 1.2
H	47.3430	123.6396	167.9	Qt7	748	55-85	3.28 + 0.36 - 0.34	3.46 + 0.69 - 0.40	0.36 + 0.15 - 0.08	0.40 + 0.10 - 0.16	WYN-04	8.9 ± 1.2
I	47.3431	123.6390	167.9	Qt7	796	55-85	2.01 + 0.72 - 0.71	2.18 + 0.83 - 0.80	0.22 + 0.13 - 0.08	0.23 + 0.15 - 0.08	WYN-04	8.9 ± 1.2
J	47.3432	123.6385	167.8	Qt7	833	55-85	2.20 + 1.10 - 1.09	2.40 + 1.25 - 1.21	0.24 + 0.17 - 0.12	0.26 + 0.19 - 0.13	WYN-04	8.9 ± 1.2
K	47.3448	123.6332	214.2	Qt4	1274	55-85	2.46 + 0.84 - 0.57	2.63 + 1.02 - 0.64	0.08 + 0.04 - 0.03	0.08 + 0.05 - 0.02	WYN-17	32.2 ± 4.8
L	47.3450	123.6324	215.1	Qt4	1338	55-85	2.87 + 0.51 - 0.47	2.98 + 0.80 - 0.48	0.09 + 0.04 - 0.03	0.09 + 0.05 - 0.02	WYN-17	32.2 ± 4.8
M	47.3452	123.6318	217.0	Qt4	1392	55-85	1.77 + 0.37 - 0.35	1.91 + 0.47 - 0.42	0.05 + 0.03 - 0.01	0.06 + 0.03 - 0.02	WYN-17	32.2 ± 4.8
N	47.3454	123.6311	219.0	Qt4	1446	55-85	1.56 + 0.33 - 0.33	1.60 + 0.52 - 0.41	0.05 + 0.02 - 0.02	0.05 + 0.03 - 0.02	WYN-17	32.2 ± 4.8
O	47.3464	123.6264	287.0	Qt4	2138	55-85	6.09 + 2.97 - 2.39	6.50 + 2.77 - 2.76	0.19 + 0.13 - 0.08	0.20 + 0.13 - 0.09	WYN-17	32.2 ± 4.8
P	47.3464	123.6260	290.0	Qt4	2166	55-85	4.27 + 0.72 - 0.72	4.29 + 0.76 - 0.74	0.12 + 0.07 - 0.02	0.13 + 0.07 - 0.03	WYN-17	32.2 ± 4.8
X (A)	47.3321	123.6534	191.0	Qt5	n/a*	55-85	7.65 + 3.57 - 3.46	8.36 + 4.08 - 3.90	0.50 + 0.31 - 0.23	0.54 + 0.34 - 0.25	WYN-06	14.8 ± 2.0
X (B)	47.3321	123.6534	191.0	Qt5/5b	n/a*	55-85	4.27 + 1.62 - 1.61	4.67 + 2.03 - 1.94	0.28 + 0.15 - 0.10	0.29 + 0.19 - 0.11	WYN-06	14.8 ± 2.0

Note: Uncertainties reported to 1 standard deviation

OSL = optically stimulated luminescene

*Profile X was not along the same scarp as profiles A-Q, and therefore does not have a distance value.

[†]Uncertainty reported to 95% confidence

[§]Terrace units do not have age constraints, so no rate values were calculated.

TABLE DR4. STRATH LOCATIONS

Valley distance (m)	Unit	Location Lat (°N)	Location Long (°W)	Elevation* (m)	Cover thickness at exposure (m)	Bedrock type	Cover material
2098	Qt7	47.3743	123.6289	182.2 ± 0.9	n/a†	Till	Gravel
2306	Qt8b	47.3728	123.6305	176.0 ± 0.8	0.0	Basalt	None
5755	Qt7	47.3423	123.6409	163.5 ± 0.2	2.8	Lacustrine	Gravel and loess
5762	Qt7	47.3422	123.6408	162.7 ± 0.2	3.0	Lacustrine	Gravel and loess
5777	Qt7	47.3420	123.6406	161.1 ± 0.3	4.0	Lacustrine	Gravel
5785	Qt7	47.3420	123.6406	160.8 ± 0.2	5.2	Lacustrine	Gravel
5952	Qt6	47.3414	123.6453	177.6 ± 0.5	2.0	Lacustrine	Gravel
7389	Qt4	47.3299	123.6441	197.9 ± 1.0	<1.0	Basalt	Soil
7525	Qt5b	47.3294	123.6428	186.6 ± 0.9	<1.0	Basalt	Gravel
8140	Qt4b	47.3231	123.6427	194.1 ± 0.3	2.3	Lacustrine over basalt	Sand and gravel
8155	Qt4b	47.3229	123.6427	192.7 ± 0.4	2.0	Lacustrine over basalt	Sand and gravel
9259	Qt4	47.3136	123.6446	191.4 ± 0.3	1.0	Basalt	Gravel and loess
11040	Qt5b	47.2997	123.6529	139.7 ± 1.7	n/a†	Basalt	Montesano Fm.
11062	Qt5b	47.2994	123.6528	147.2 ± 3.2	2.9	Montesano Fm.	Gravel and loess
21000	Qt6	47.2115	123.6335	94.0 ± 1.1	3.5	Montesano Fm.	Gravel
21105	Qt6c	47.2117	123.6292	84.9 ± 0.3	1.5	Montesano Fm.	Gravel and soil
26695	Qt5	47.1649	123.6335	84.9 ± 0.2	5.1	Montesano Fm.	Gravel and loess
29607	Qt2b	47.1393	123.6372	79.0 ± 1.0	2.0	Montesano Fm.	Gravel
30524	Qt5	47.1293	123.6415	71.1 ± 1.3	3.3	Montesano Fm.	Gravel and soil
34102	Qt5	47.1045	123.6718	59.5 ± 0.7	1.0	Montesano Fm.	Gravel
34980	Qt5b	47.1005	123.6850	51.1 ± 0.2	3.2	Montesano Fm.	Gravel and loess
35059	Qt5b	47.0999	123.6854	50.8 ± 0.3	2.5	Montesano Fm.	Gravel and loess
35161	Qt5b	47.0989	123.6856	51.0 ± 0.3	2.5	Montesano Fm.	Gravel and loess
39756	Qt5	47.0586	123.6929	38.9 ± 0.2	3.1	Montesano Fm.	Gravel and loess
39803	Qt5	47.0582	123.6927	38.8 ± 0.2	3.1	Montesano Fm.	Gravel and loess
40372	Qt5c	47.0531	123.6920	34.7 ± 0.6	1.5	Montesano Fm.	Gravel
41332	Qt5	47.0441	123.6970	32.8 ± 0.6	n/a†	Montesano Fm.	Gravel and soil
42734	Qt5	47.0308	123.6989	30.5 ± 0.8	3.0	Montesano Fm.	Gravel and soil
43858	Qt5b	47.0208	123.6968	27.3 ± 1.8	1.8	Montesano Fm.	Soil
45057	Qt5	47.0064	123.6878	§24.3 ± 0.2	7.0	Montesano Fm.	Gravel
46339	Qt5	47.0003	123.6734	§18.7 ± 0.2	4.6	Montesano Fm.	Gravel
49802	Qt8	46.9715	123.6262	2.0 ± 0.5	2.4	Montesano Fm.	Gravel

*Errors reported to 1 standard deviation.

†Cover thickness could not be measured in the field due to lack of visibility of the tread surface

§Well log data

TABLE DR5. QT5 STRATH INCISION AND INCISION RATES

Valley distance (km)	Strath height ± 1σ (m)			Qt5 age ± 1σ (ka)			Incision rate ± 2σ (mm/yr)		
0.0	36.3 +	1.0 -	1.0	14.1 ±	0.6		2.57 +	0.3 -	0.3
2.0	31.7 +	1.0 -	13.0	14.1 ±	0.6		2.25 +	0.2 -	1.9
6.0	22.8 +	3.0 -	3.0	14.1 ±	0.6		1.62 +	0.4 -	0.4
7.3	20.8 +	3.5 -	3.5	14.1 ±	0.6		1.48 +	0.5 -	0.5
7.5	45.1 +	2.7 -	2.7	14.1 ±	0.6		3.20 +	0.5 -	0.5
8.1	45.7 +	2.2 -	2.2	14.1 ±	0.6		3.24 +	0.4 -	0.4
10.4	38.0 +	4.0 -	4.0	14.1 ±	0.6		2.70 +	0.6 -	0.6
11.1	29.0 +	3.5 -	3.5	14.1 ±	0.6		2.06 +	0.5 -	0.5
21.0	12.7 +	5.0 -	1.1	14.1 ±	0.6		0.90 +	0.7 -	0.2
26.6	23.4 +	0.2 -	0.2	14.1 ±	0.6		1.66 +	0.1 -	0.1
30.5	26.8 +	1.3 -	1.3	14.1 ±	0.6		1.90 +	0.2 -	0.2
34.1	24.1 +	0.7 -	0.7	14.1 ±	0.6		1.71 +	0.2 -	0.2
39.8	15.8 +	0.2 -	0.2	14.1 ±	0.6		1.12 +	0.1 -	0.1
41.3	12.5 +	0.6 -	0.6	14.1 ±	0.6		0.89 +	0.1 -	0.1
42.7	12.7 +	0.8 -	0.8	14.1 ±	0.6		0.90 +	0.1 -	0.1
43.8	12.8 +	1.8 -	1.8	14.1 ±	0.6		0.91 +	0.3 -	0.3
45.0	*11.5 +	0.2 -	0.2	14.1 ±	0.6		0.82 +	0.1 -	0.1
46.0	*9.7 +	0.2 -	0.2	14.1 ±	0.6		0.69 +	0.1 -	0.1
49.8	6.0 +	4.0 -	3.0	14.1 ±	0.6		0.43 +	0.6 -	0.4

*Strath data from well logs

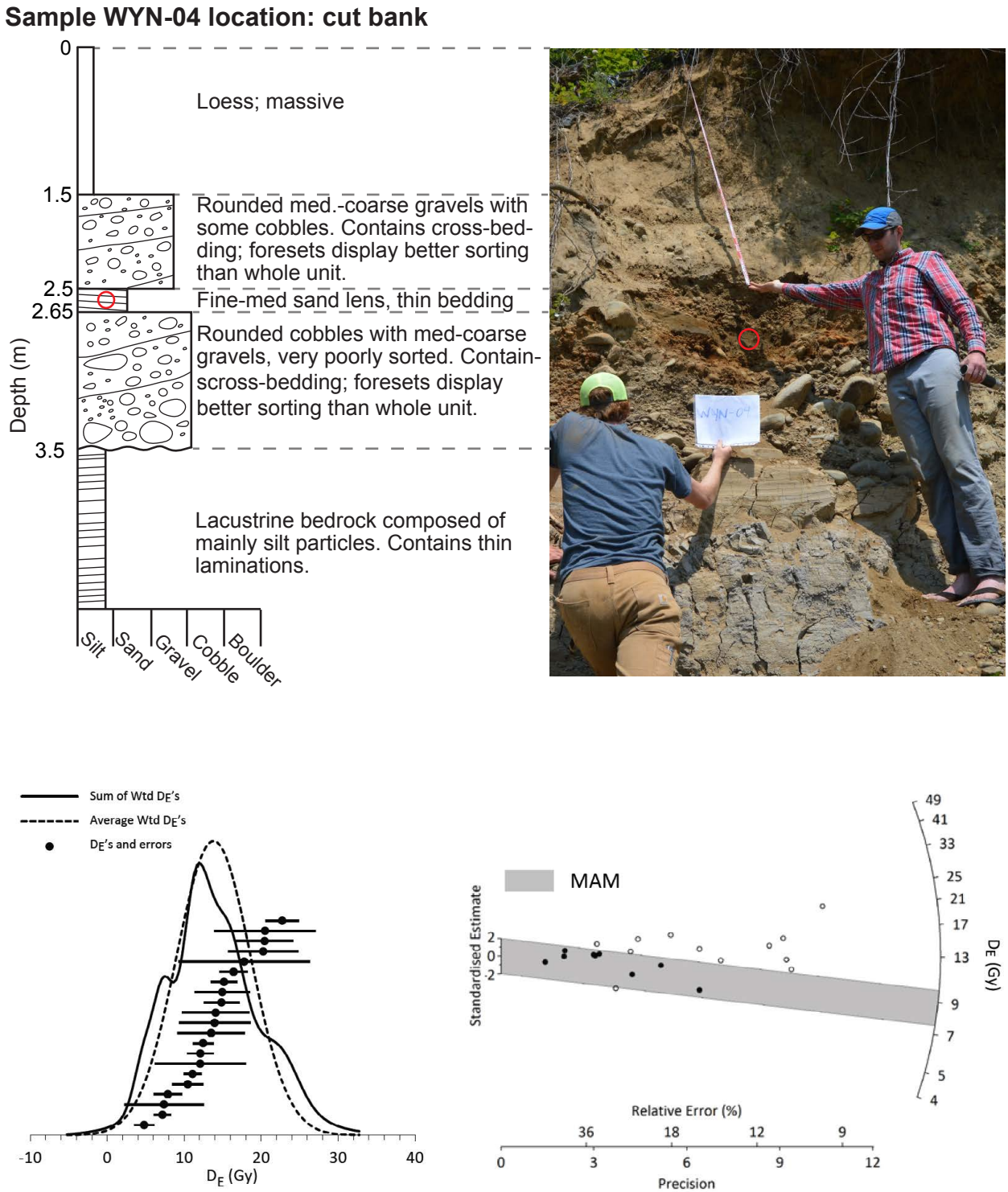

Figure DR1. Stratigaphic column for sample site and equivalent dose probability density functions and radial plots of sample WYN-04.

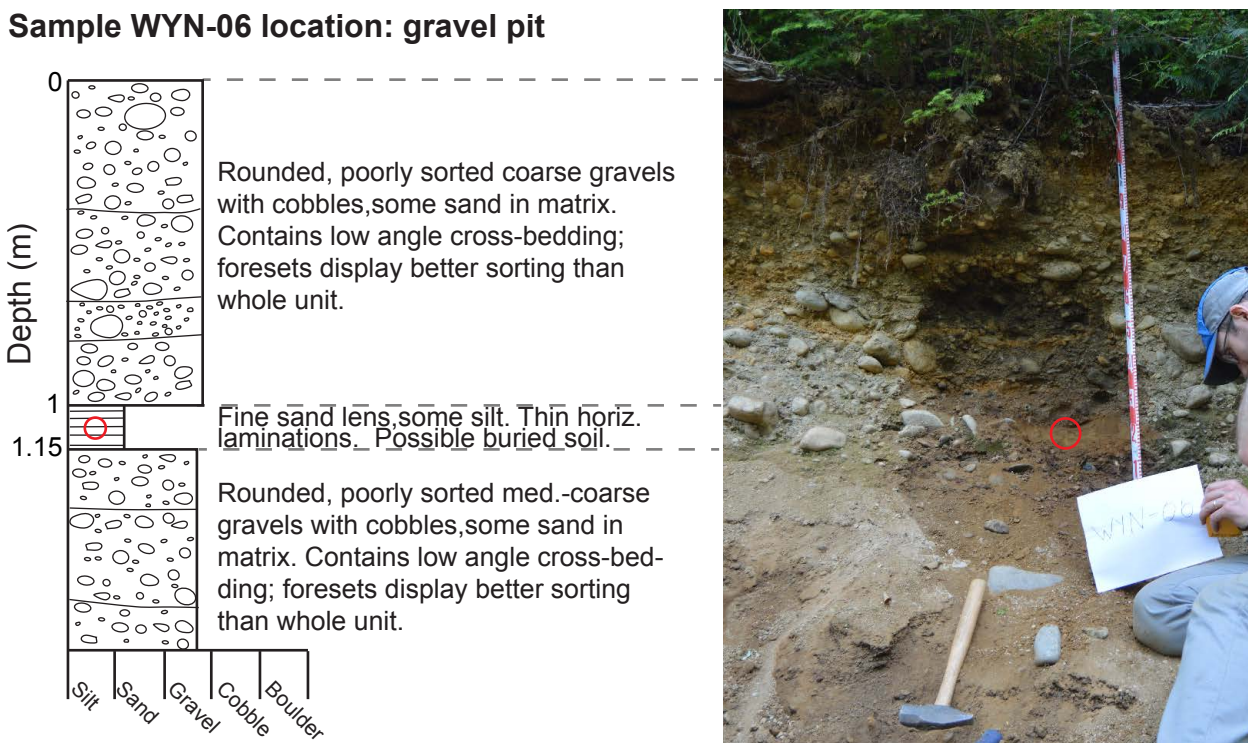

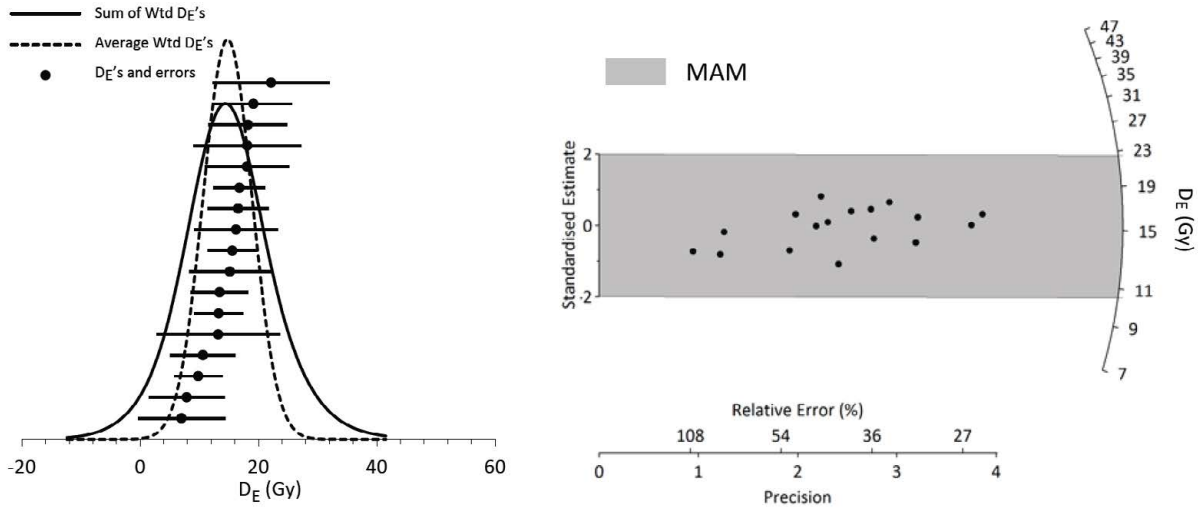

Figure DR2. Stratigaphic column for sample site and equivalent dose probability density functions and radial plots of sample WYN-06.

Sample WYN-07 location: Exposed cliff adjacent to road (old river cutbank)

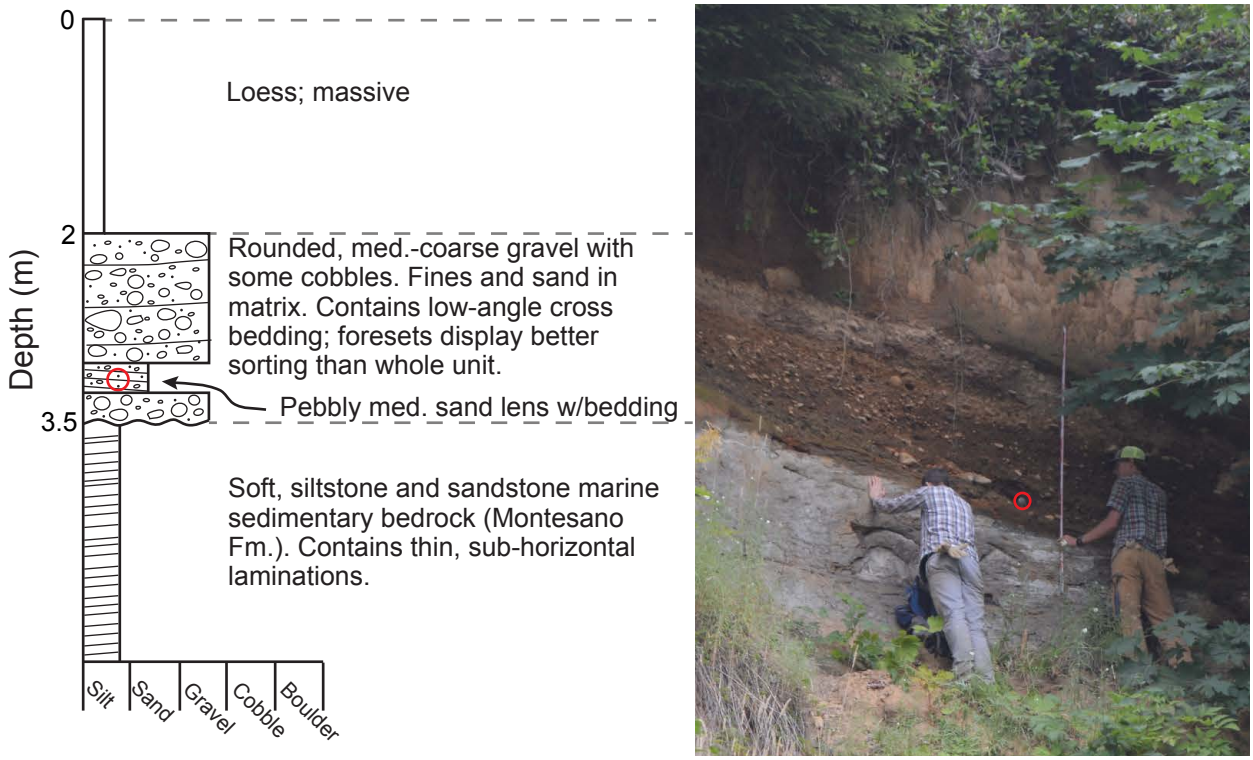

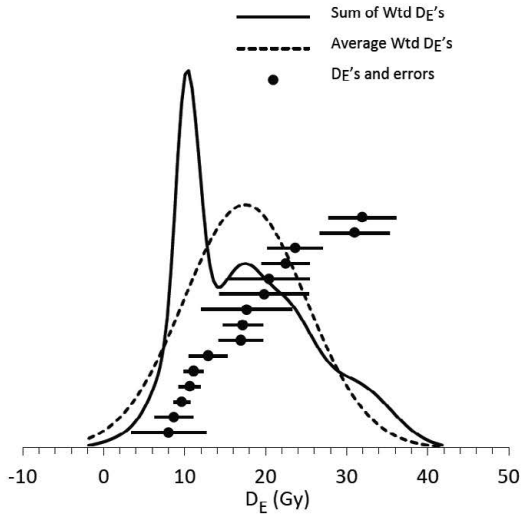

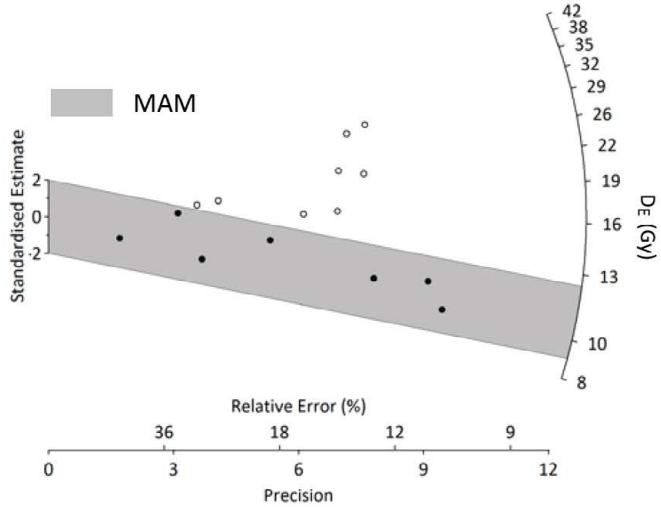

Figure DR3. Stratigaphic column of sample site and equivalent dose probability density functions and radial plot of sample WYN-07.

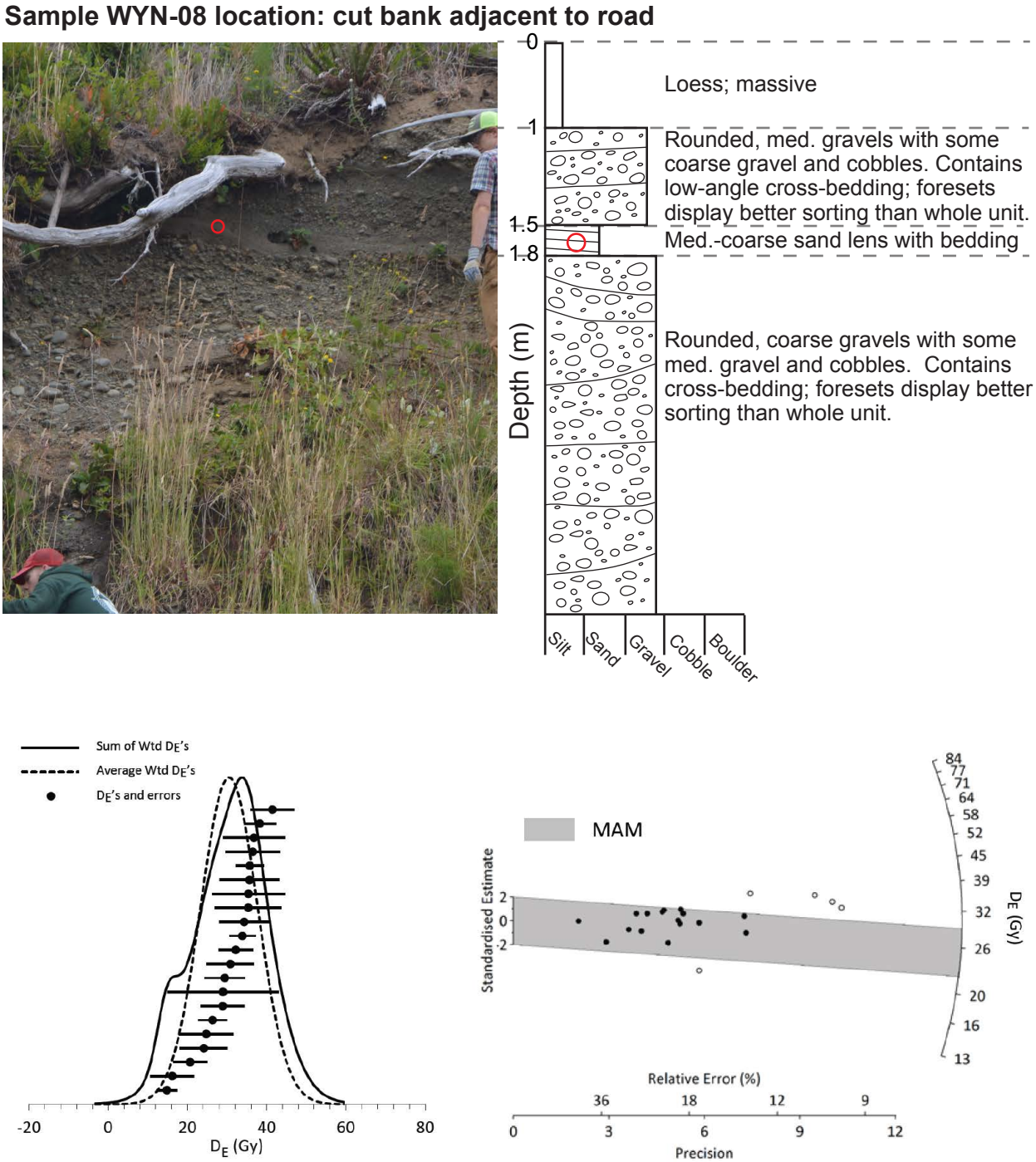

Figure DR4. Stratigaphic column for sample site and equivalent dose probability density functions and radial plots of sample WYN-08.

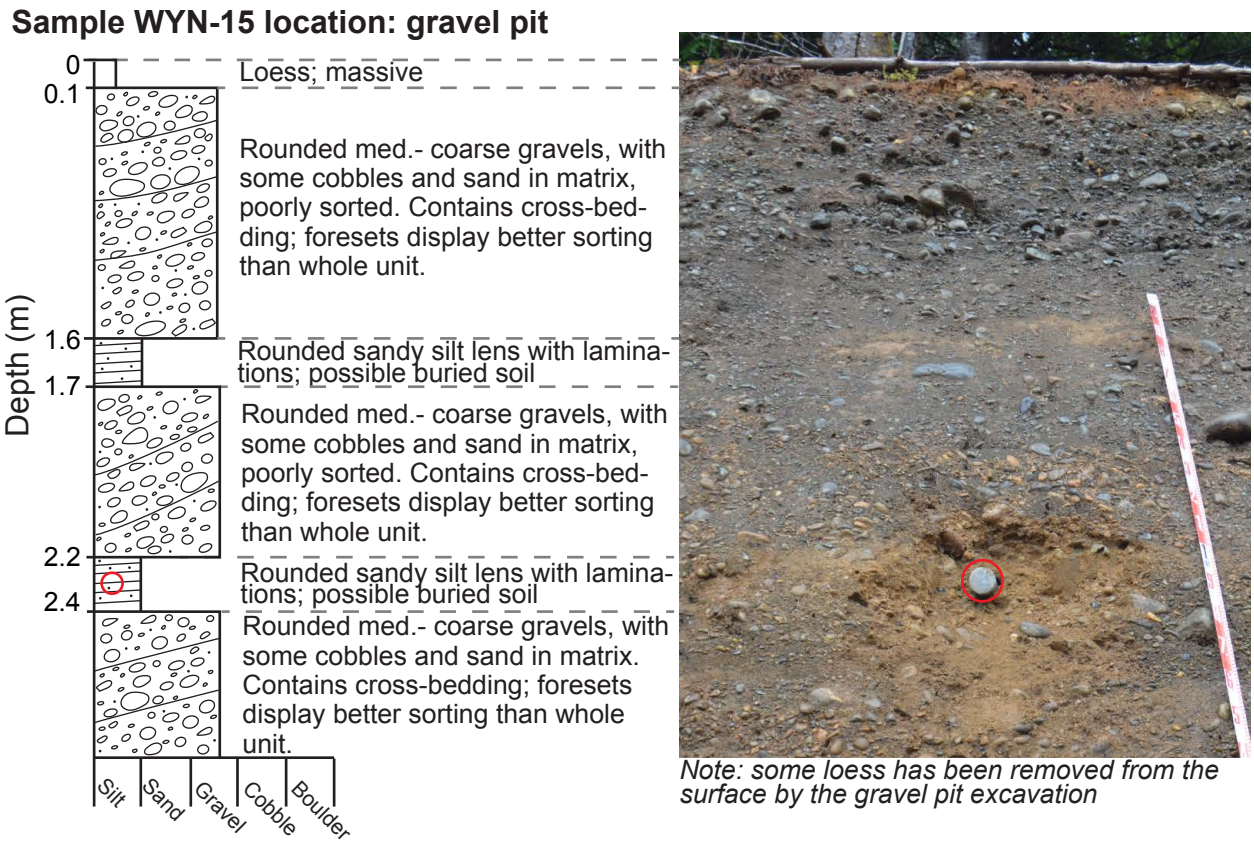

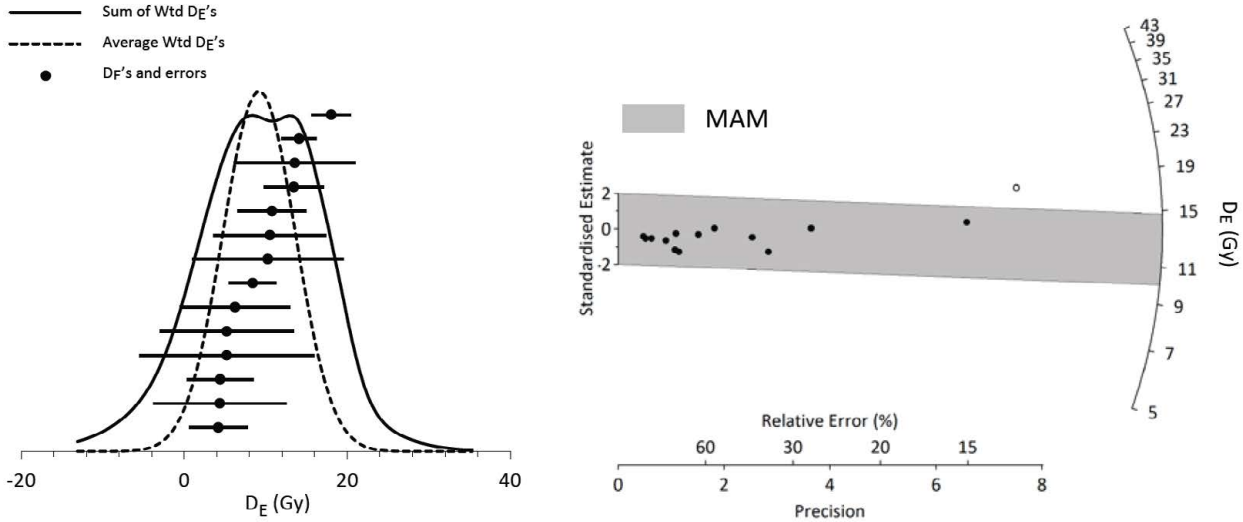

Figure DR5. Stratigaphic column for sample site and equivalent dose probability density functions and radial plots of sample WYN-15.

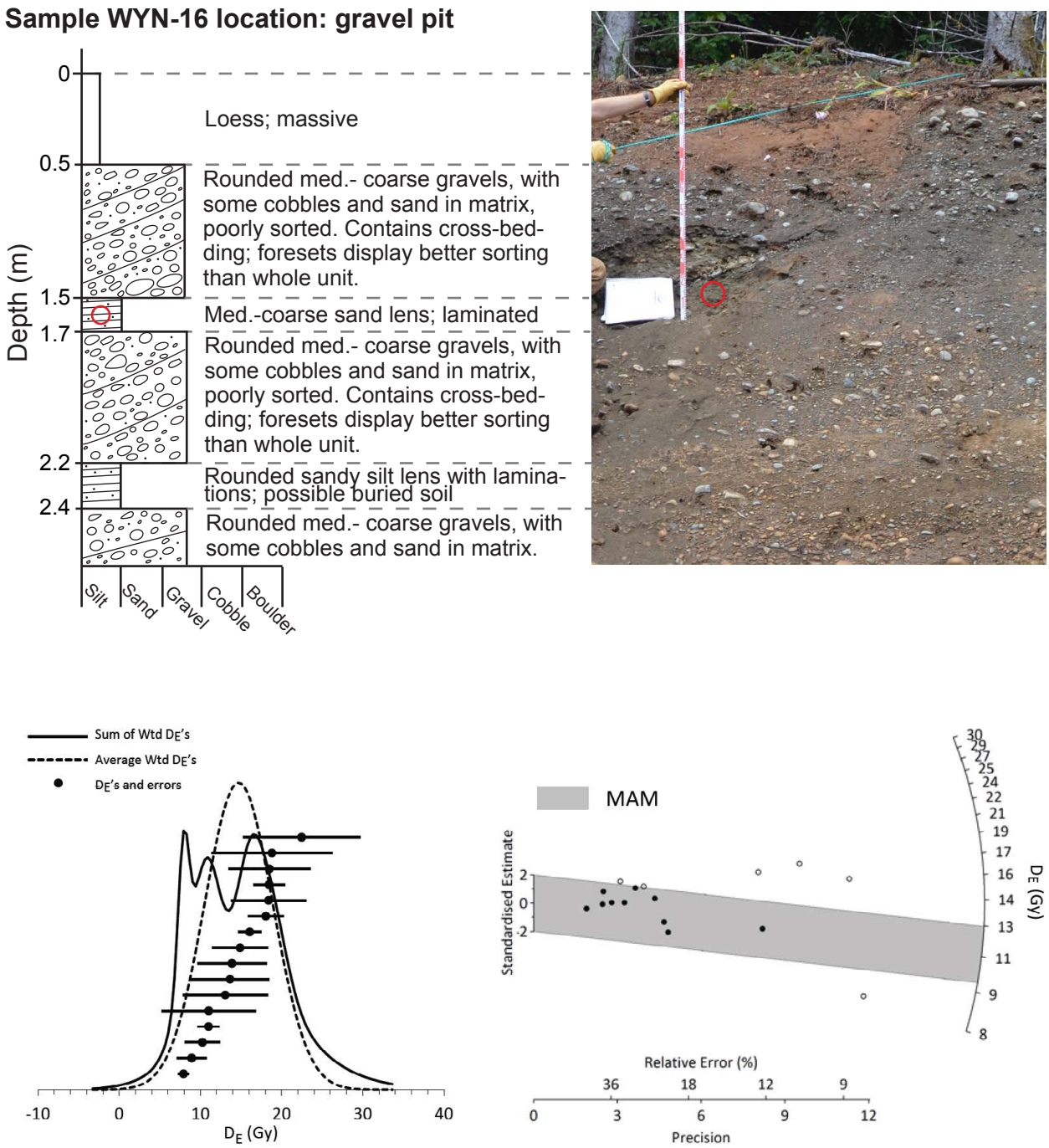

Figure DR6. Stratigaphic column for sample site and equivalent dose probability density functions and radial plots of sample WYN-16.

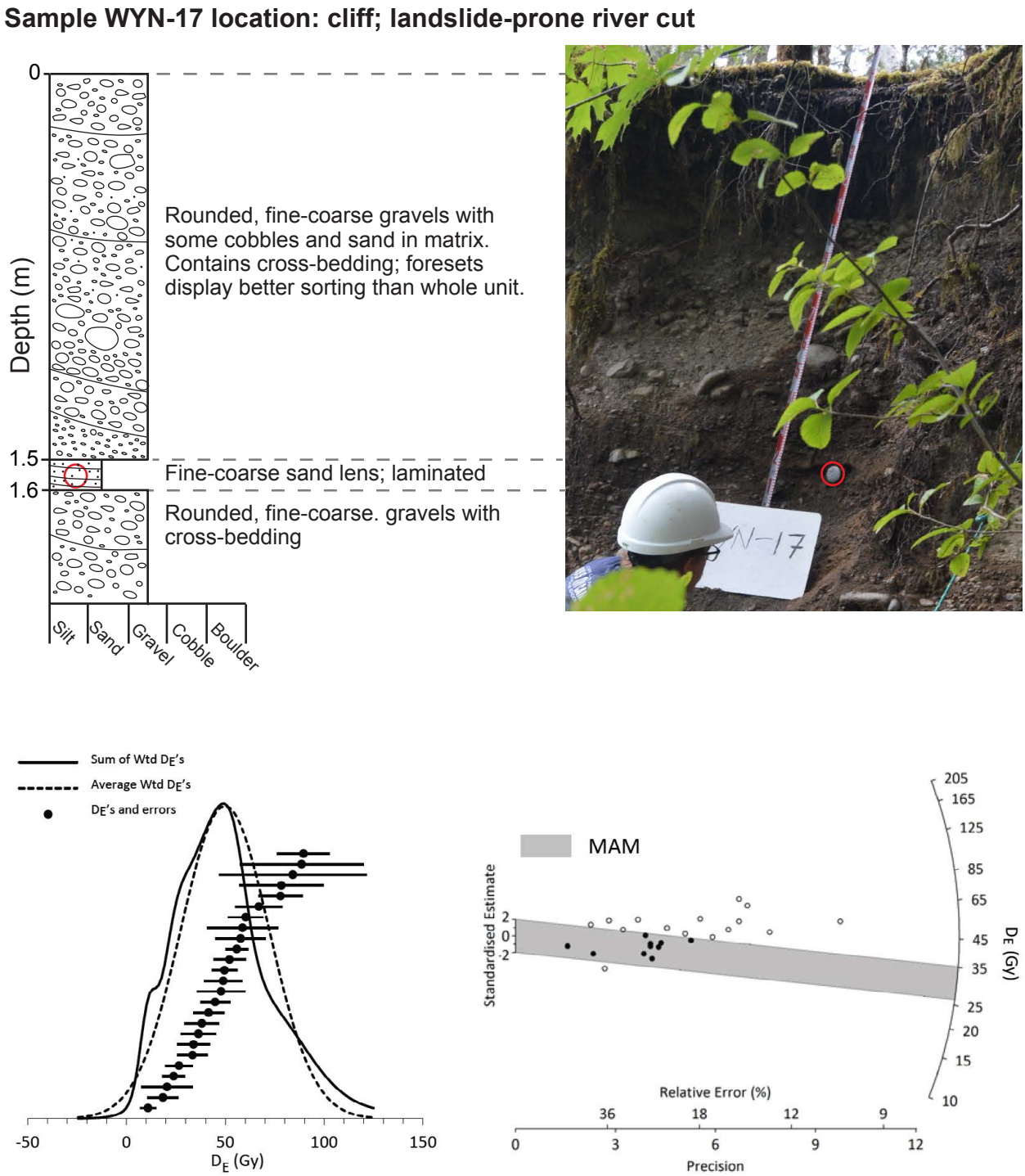

Figure DR7. Stratigaphic column for sample site and equivalent dose probability density functions and radial plots of sample WYN-17.

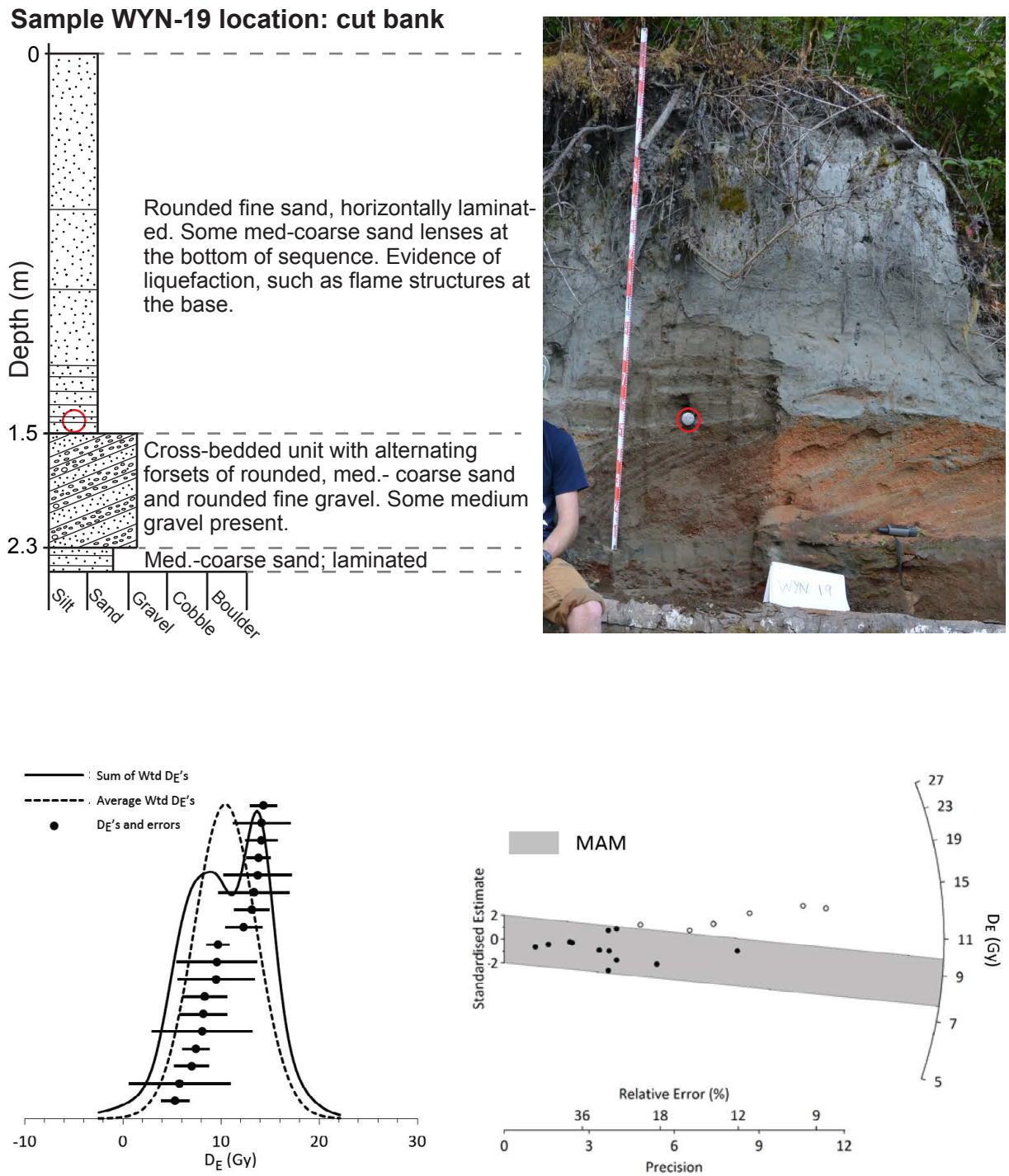

Figure DR8. Stratigaphic column for sample site and equivalent dose probability density functions and radial plots of sample WYN-19.

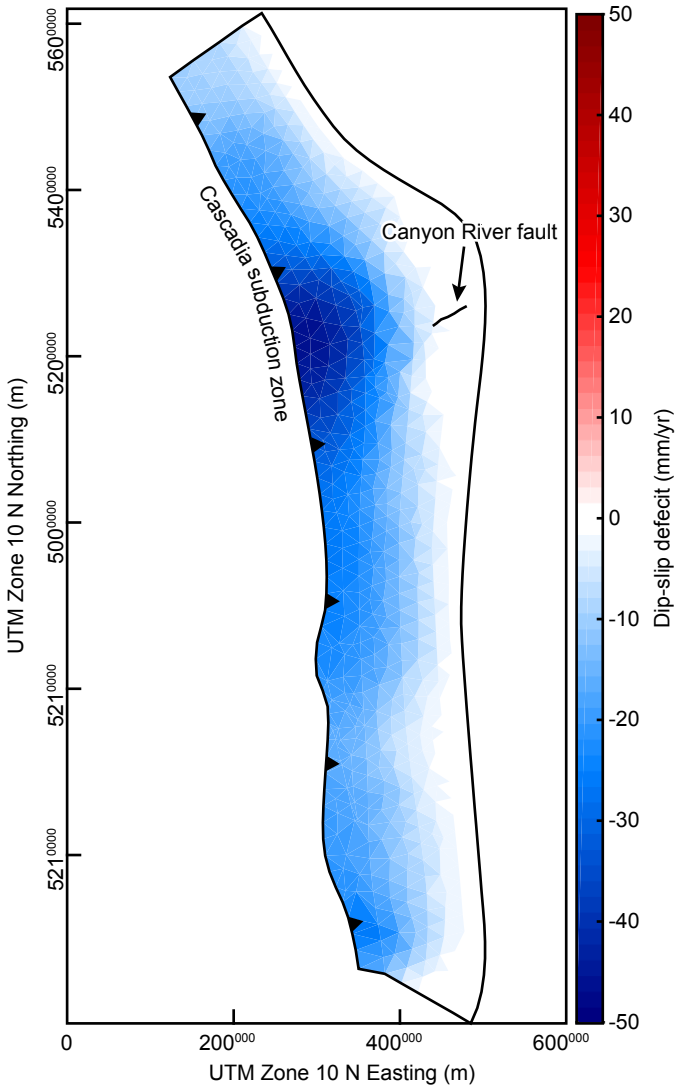

Figure DR9. Dip-slip deficit distribution on the Cascadia subduction zone slab interface, constrained by GPS. Barbs on subduction zone point down dip.

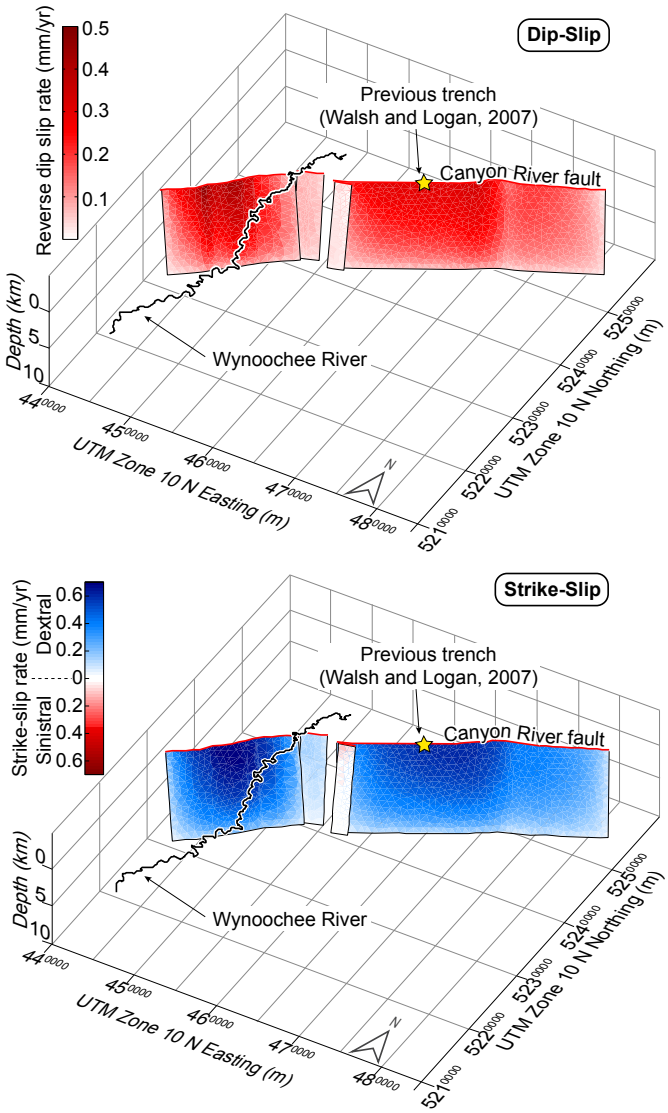

Figure DR10. Dip slip and strike-slip rate results on the Canyon River fault from the boundary element model using 70° dip, projected to 10 km depth.

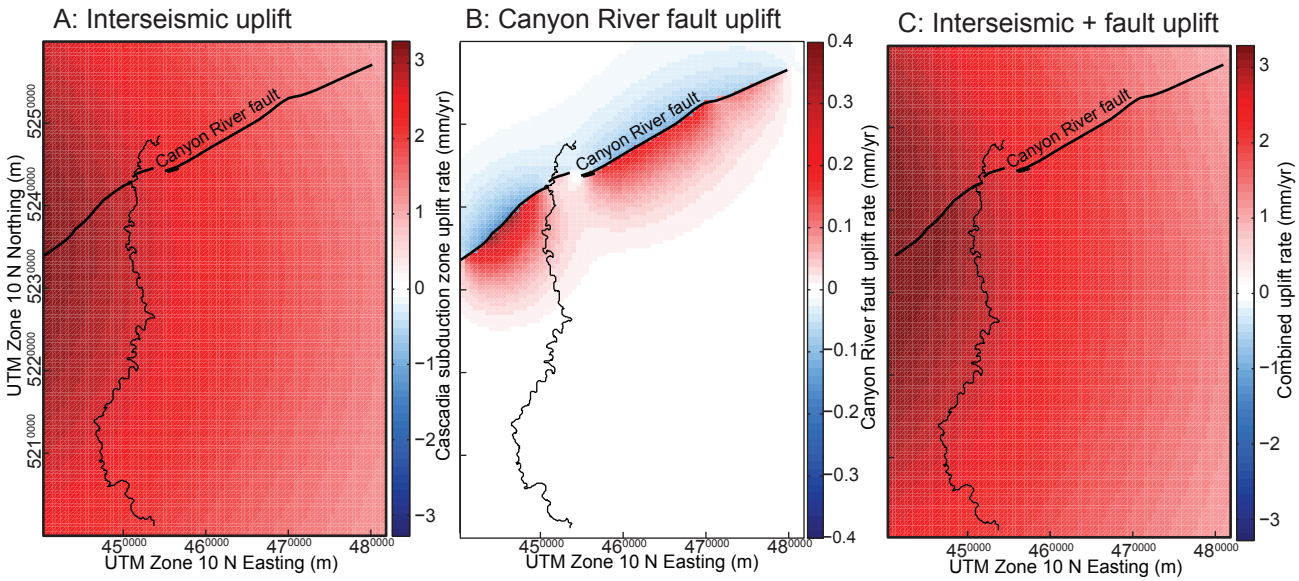

Figure DR11. Regional uplift maps of the Wynoochee River from estimated from the boundary element model. A) Estimated uplift from interseismic deformation on the coupled Cascadia subduction zone. B) Estimated uplift pattern from time-averaged slip on the Canyon River fault. C) Combined uplift from A and B.

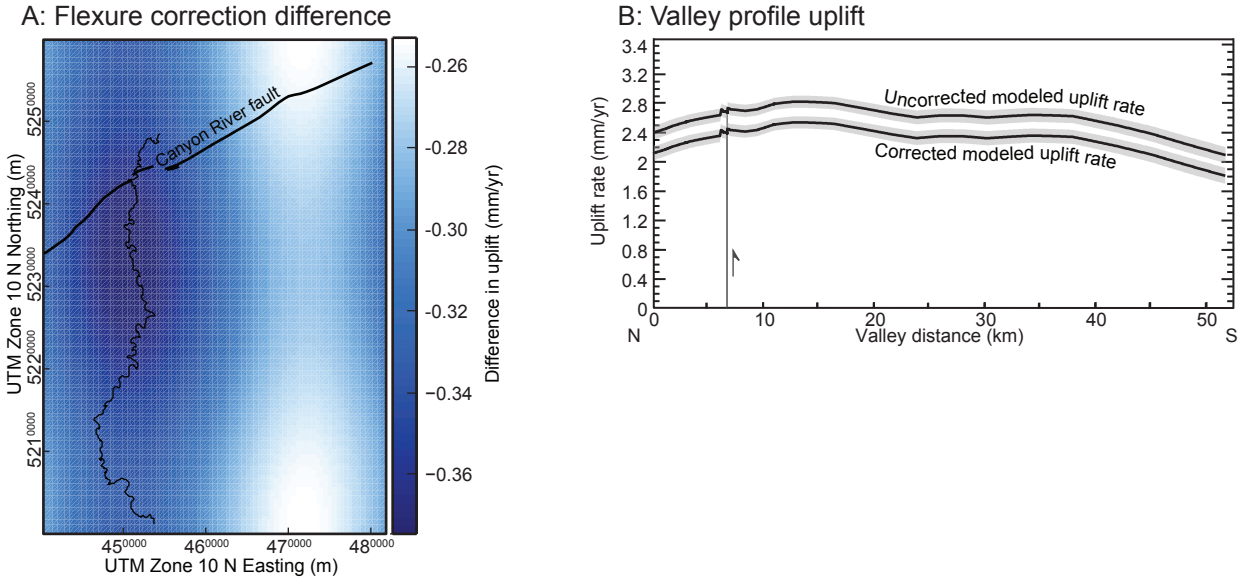

Figure DR12. Uplift differences from the flexure correction (see Appendix DR1) A) Cascadia subduction zone uplift difference between corrected and uncorrected models. B) Variation in combined uplift of interseismic and fault slip resulting from flexure correction.

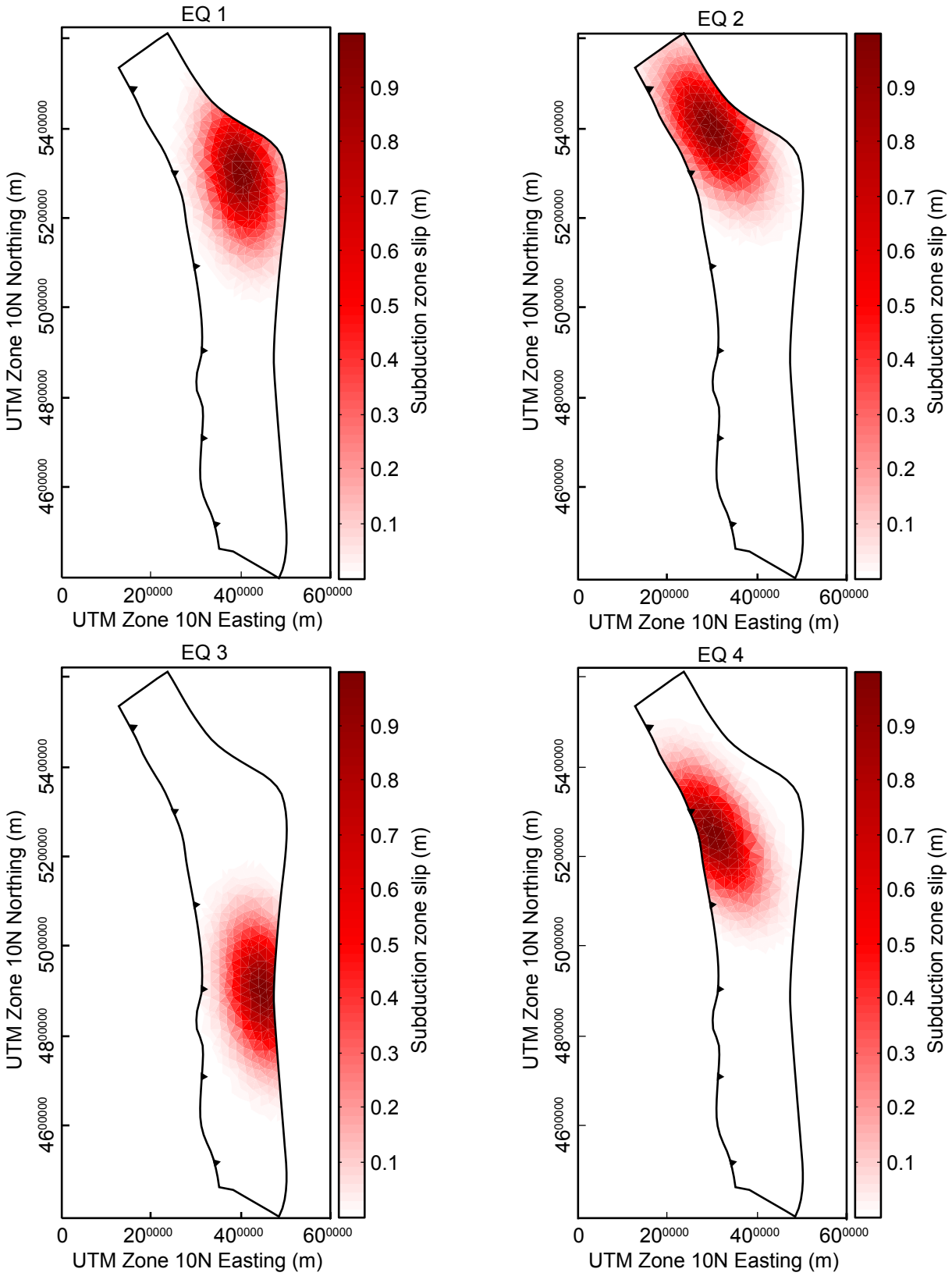

Figure DR13. Synthetic earthquake dip-slip on the Cascadia subduction zone interface with 1 m peak slip. Resulting slip configurations on the Canyon River fault shown in Figure DR14.

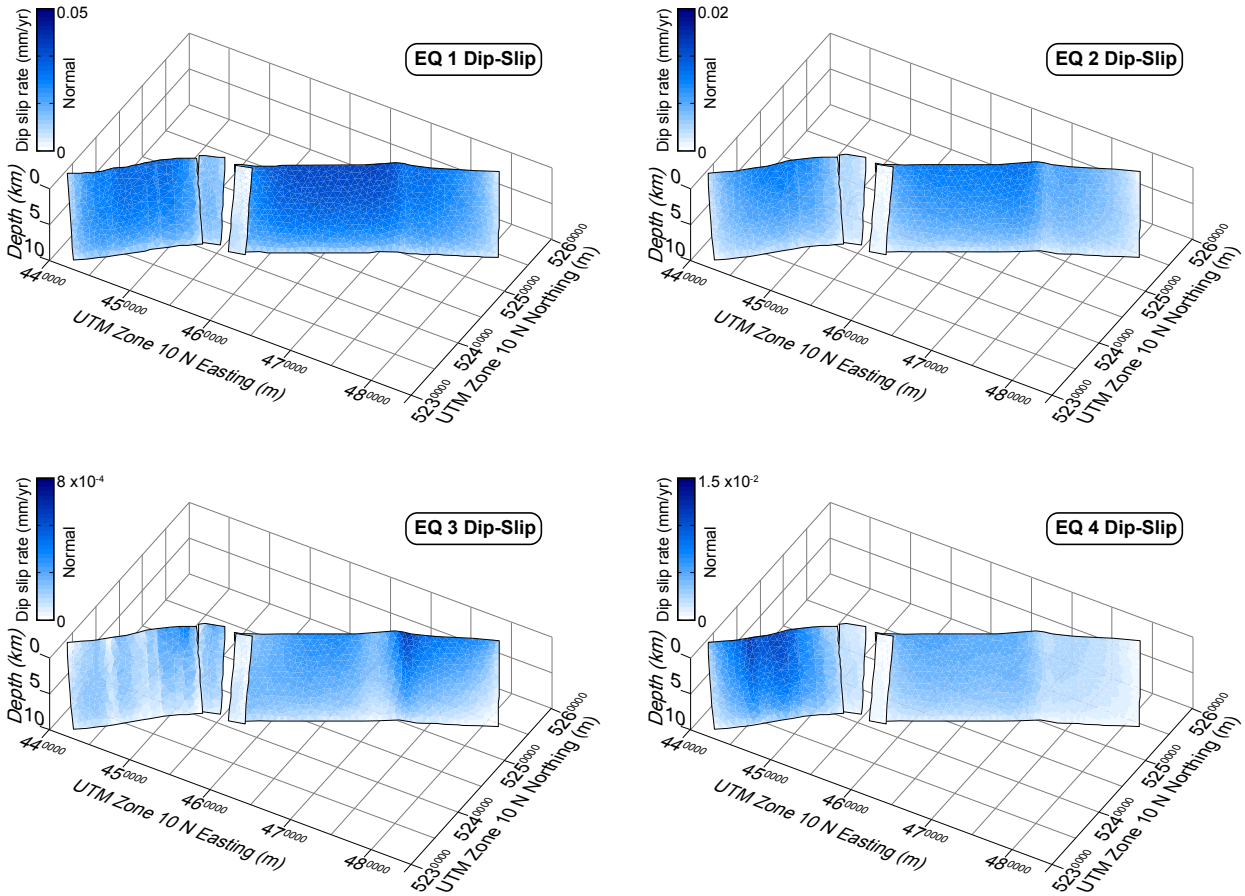

Figure DR14. Slip on the Canyon River fault resulting from synthetic earthquake slip on the Cascadia subduction zone interface. Cascadia subduction slip configurations shown in Figure DR13.